Article

A Sensitive and Selective Non-Enzymatic Dopamine Sensor Based on Nanostructured Co_3O_4–Fe_2O_3 Heterojunctions

Madiha Khan [1,2], Khouloud Abid [1,3], Angelo Ferlazzo [1], Viviana Bressi [1], Claudia Espro [1], Mozaffar Hussain [2], Antonino Foti [3], Pietro Giuseppe Gucciardi [3] and Giovanni Neri [1,*]

1   Department of Engineering, University of Messina, C.da Di Dio, I-98166 Messina, Italy;
     madihakhan@students.au.edu.pk (M.K.); khouloud.abid@studenti.unime.it (K.A.);
     angelo.ferlazzo@unime.it (A.F.); vibressi@unime.it (V.B.); claudia.espro@unime.it (C.E.)
2   Department of Physics, Air University, PAF Complex, E-9, Islamabad 4400, Pakistan;
     mozaffarhussain@mail.au.edu.pk
3   CNR IPCF Istituto per i Processi Chimico-Fisici, Viale F. Stagno D'Alcontres 37, I-98156 Messina, Italy;
     foti@ipcf.cnr.it (A.F.); gucciardi@ipcf.cnr.it (P.G.G.)
*   Correspondence: giovanni.neri@unime.it

Abstract: In the present work, a study was carried out with the aim of enhancing the performance of electrochemical biosensors based on Co_3O_4:Fe_2O_3 heterojunctions. Specifically, the redox behavior of screen–printed carbon electrodes (SPCEs) modified with Co_3O_4:Fe_2O_3 (0.5 wt%:x wt%) nanocomposites, where x ranged from 0.1 to 0.5 wt%, was examined in detail. The hybrid nanocomposites were synthesized using the sol-gel auto-combustion method. Several characterization methods were performed to investigate the morphology, microstructure, and surface area of the pure Co_3O_4, pure Fe_2O_3, and the synthesized Co_3O_4:Fe_2O_3 nanocomposites. Using cyclic voltammetry (CV) tests, the electrochemical behavior of the modified electrodes toward the dopamine (DA) molecules was investigated. The modified Co_3O_4:Fe_2O_3, (0.5 wt%, x = 0.4 wt%)/SPCE resulted in a sensor with the best electrochemical performance toward DA. A high linear relationship between DA concentrations and the faradic current variation (i_{pa} (μA) = 0.0736 + 0.1031 C_{DA} (μA) and R^2 = 0.99) was found in the range of 10–100 μM. The sensitivity value was computed to be 0.604 μA $\mu M^{-1}cm^{-2}$ and the limit of detection (LOD) 0.24 μM. Based on the characterization and electrochemical results, it can be suggested that the formation of Co_3O_4:Fe_2O_3 heterostructures provides a large specific surface area, an increased number of electroactive sites at the metal oxide interface and a p–n heterojunction, thus ensuring a remarkable enhancement in the electrochemical response towards DA.

Keywords: metal oxide; nanocomposites; dopamine electrochemical detection; biosensors

1. Introduction

Dopamine (DA) is a neurotransmitter secreted directly by the brain, capable of activating cellular response. It is also related to spreading pleasure and the habit of drugs. Low levels of DA are responsible for the onset of diseases such as Parkinson's disease. Accumulation can also lead to numerous diseases, such as cardiovascular disease, Alzheimer's disease, and cancer [1–4]. Thus, it is fundamental to detect DA precisely and efficiently. Numerous approaches have been established to identify this biomolecule, including photoluminescence, spectrophotometry, electrochemical sensors, and chemoluminescence [5]. Electrochemical sensors appeal to our consideration because of their high sensitivity, low cost, and time-saving features [6].

There are various enzyme-based electrochemical sensors in the literature for the determination of DA [7] and its precursors, such as tyrosine [8] and phenylalanine [9], but all of them show difficulties in use, due to the presence of the enzymes themselves. For this reason, alternative materials for the development of these sensors are much studied.

In recent times, screen-printed carbon electrode (SPCE) electrochemical sensors have been largely used in different fields such as in medicine, the environment and so on [10,11]. The SPCE based on heterostructures and nano-heterojunction derivatives that are based on metal oxides (MOs) has received great interest. Furthermore, the use of screen-printed carbon electrodes (SPCEs) as transducer substrates for electrochemical sensors represent a key point in today's technology since these devices are well known to be cheap and suitable for low-cost mass production. In addition, these electrodes can be easily modified by suitable electrocatalysts, which greatly enhances the sensing capability of SPCEs utilized for the detection of different analytes. Further, they fit easily when applied to the point-of-care field, being portable and completely operated by the patients themselves.

The use of metal oxides for sensing was restricted for many decades to detect gaseous species [12]. However, in the last decades, their application in electrochemical sensors for developing enzyme-free devices has grown in an accelerated manner [13]. Indeed, nowadays, they play a prominent role for the development of novel sensors, exhibiting better properties due to their high conductivity, fast charge mobility, and large specific area, along with strong mechanical and thermal characteristics. Further, these nanostructures can provide enhanced electrocatalytic properties towards many biomolecules of interests.

Composites based on metal oxides, such as cobalt oxide (Co_3O_4), and iron oxide (Fe_2O_3), are gaining a lot of attention for sensing applications. Pristine cobalt and iron oxide, prepared by the thermal stirring method, have superior conductivity due to better preservation of material structures [14,15]. Further, Co_3O_4:Fe_2O_3 nanocomposites may exhibit good electrochemical performances [16]. For example, these nanocomposites are among the most attractive materials owing to their unique peroxidase-like activity [17]. Many methods are used to prepare Co_3O_4:Fe_2O_3 nanocomposites, including the hydrothermal reaction method, ultrasonic chemical method, micro-emulsion method, co-precipitation method, iron salt high-temperature pyrolysis method, and so on [18,19]. Among these, sol-gel is the most conventional method [20].

In this paper, we synthesized pure Co_3O_4 and Fe_2O_3 nanoparticles by the co-precipitation method and then, by using the sol-gel auto-combustion method, obtained the Co_3O_4:Fe_2O_3 nanocomposites, varying the Co_3O_4 and Fe_2O_3 nanoparticle ratio. The structural, morphological, and optical properties of cobalt oxide-loaded iron oxide were studied. Nanocomposites with different Co_3O_4:Fe_2O_3 ratios (0.5 wt%: x = 0.1, 0.2, 0.3, 0.4, 0.5 wt%) were employed for the detection of DA using cyclic voltammetry as an electrochemical technique. Even if DA detection is, as above mentioned, of outmost importance in clinical medicine, here, our main objective was to study the electrochemical performances of the developed sensors based on Co_3O_4:Fe_2O_3 heterojunctions towards dopamine, chosen as a model compound. To our best knowledge, there is no work reporting this composite formulation in electrochemical sensors.

The electrochemical tests of a screen-printed electrode modified with Co_3O_4:Fe_2O_3 nanocomposites demonstrate that they could efficiently detect dopamine better than the bare SPCE and modified Co_3O_4/SPCE and Fe_2O_3/SPCE. The results obtained from the tests conducted, indicated Co_3O_4:Fe_2O_3 (0.1 wt%:0.4 wt%) as the best nanocomposite heterostructure for DA electroanalytical determination.

2. Materials and Methods

2.1. Materials

Cobalt oxide nanoparticles (Co_3O_4), and hematite iron oxide nanoparticles (Fe_2O_3), were prepared by using pure grade nitrates (99.99%) supplied by Sigma Aldrich Italy.

2.2. Synthesis of Co_3O_4:Fe_2O_3 Nanocomposites

Co_3O_4:Fe_2O_3 nanocomposites with different Co_3O_4 and Fe_2O_3 ratios (0.5 wt%: x = (0.1, 0.2, 0.3, 0.4 and 0.5 wt%)) were synthesized by using a two-step procedure. First, the pure Co_3O_4 and Fe_2O_3 materials were prepared by the precipitation method. Co_3O_4 was dissolved in hydrochloric acid (HCl) and continuously stirred at room temperature

until the solution became transparent and uniform. Then, various quantities of hematite (from 0.001 to 0.005 mol) were dissolved in 5 M citric acid (HOC(CO$_2$H) (CH$_2$CO$_2$H)$_2$) solution and stirred at room temperature till the solution became transparent and uniform. Subsequently, Co$_3$O$_4$ and Fe$_2$O$_3$ solutions were mixed and placed on a heating plate at a temperature of ~350 °C. The materials were fully burned, obtaining five samples with different Fe$_2$O$_3$/Co$_3$O$_4$ molar ratios. Finally, the powdered samples were annealed in a glass furnace for 2 h at 400 °C. The five samples were identified as

$$x = Fe_2O_3/y = Co_3O_4,$$

where x and y indicate the molar composition of two components (i.e., 0.2Fe$_2$O$_3$/1Co$_3$O$_4$, 0.4Fe$_2$O$_3$/1Co$_3$O$_4$, 0.6Fe$_2$O$_3$/1Co$_3$O$_4$, 0.8Fe$_2$O$_3$/1Co$_3$O$_4$, 1Fe$_2$O$_3$/1Co$_3$O$_4$). The Fe$_2$O$_3$ molar % was calculated as:

$$Fe_2O_3 \text{ (molar \%)} = [(mol\ Fe_2O_3/(mol\ Fe_2O_3 + mol\ Co_3O_4)) \times 100].$$

2.3. Characterization Methods

X-ray powder diffraction (XRD) analysis was performed using a D2 Phaser Bruker diffractometer operating at 30 kV in the range 10–90° (2-θ), at a scanning rate of 0.02° s^{-1}. Scanning electron microscopy (SEM) images were acquired by Zeiss 1540XB FE SEM (Zeiss, Germany) instrument operating at 10 kV. The B.E.T. surface area and porosity of samples were evaluated by nitrogen adsorption and desorption isotherm carried out at 77 K by a Quantachrome ASiQwin instrument (Anton Paar Companies, Graz, Austria). The samples were dried at 100 °C and degassed for 2 h, before starting the analysis. Fourier transform infrared spectroscopy (FT-IR) spectra were collected by a Perkin Elmer Spectrum 100 spectrometer equipped with a universal ATR sampling. Raman spectra were collected with an XploRA Plus microspectrometer (Horiba, Kyoto, Japan) equipped with a diode laser emitting at 638 nm. The measurements were performed at room temperature using a 100× microscope objective (Olympus M-Plan, NA = 0.90, WD = 210 μm), both for excitation and collection of the scattered signal, which was dispersed by 1200 grating onto a CCD detector (Syncerity, Horiba).

2.4. Electrode Fabrication

Commercial screen-printed carbon electrodes (SPCEs) were purchased from Dropsens, Spain. The basic sensing electrodes used (DRP-100, named SPCE) were composed of a 4 mm diameter carbon working electrode, a silver pseudo-reference electrode, and a carbon auxiliary electrode. The electrodes were then modified with pure Co$_3$O$_4$, pure Fe$_2$O$_3$, and Co$_3$O$_4$:Fe$_2$O$_3$ composites. The appropriate modification amount was 50μL which was determined by the study of different amounts (30 μL, 50 μL, 70 μL, 100 μL). Then, the Co$_3$O$_4$:Fe$_2$O$_3$ nanocomposite material was sonicated in water (1 mg/1μL) and ultrapure water successively for 15 min. Then, typically, 30 and 50 μL of Co$_3$O$_4$:Fe$_2$O$_3$ nanocomposite (1 mg/1μL) were dropped on the SPCE surface and dried at room temperature overnight, as shown in Figure 1.

2.5. Electrochemical Tests

Electrochemical analyses were conducted with a DropSens μStat 400 potentiostat, using Dropview 8400 software for data processing. Electrical impedance spectroscopy (EIS) analyses were performed using a potentiostat Galvanostat by Metrohom autolab. The electrochemical tests for dopamine were performed in 10 mL of 0.01 M phosphate buffer solution (PBS, pH = 7.4) containing 0.0076 g (5 mM) of DA. The CV tests were performed in the potential range [−0.2 V to −0.8 V] at 0.05 V/s scan rate on unmodified and modified SPCEs in PBS solution containing DA at different concentrations ranging from 0 to 100 μM. Five different samples from the same batch and two pure samples were analyzed using the same procedure.
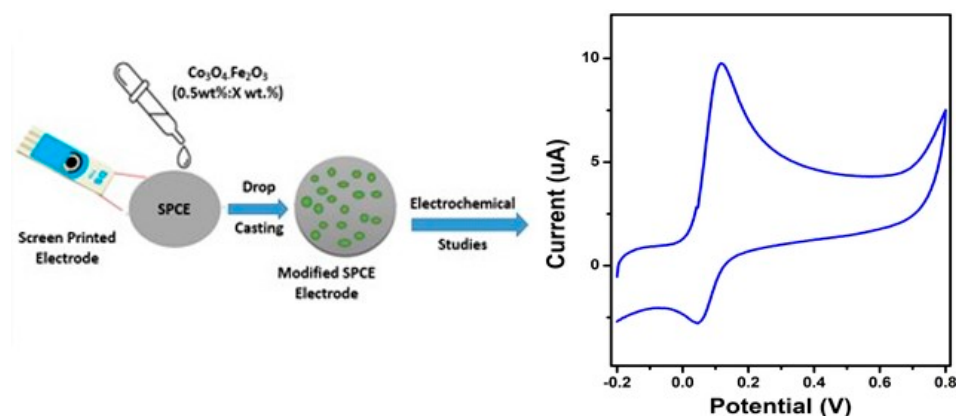
Figure 1. SPCE modification process using Co_3O_4:Fe_2O_3 nanocomposites and CV response toward the determination of DA.

3. Results and Discussion

3.1. Structural and Morphological Characterization

In Figure 2, an example of the characterizations carried out by XRD, SEM and EDX is presented, which revealed the typical structure and morphology of the synthesized Fe_2O_3:Co_3O_4 nanocomposites.
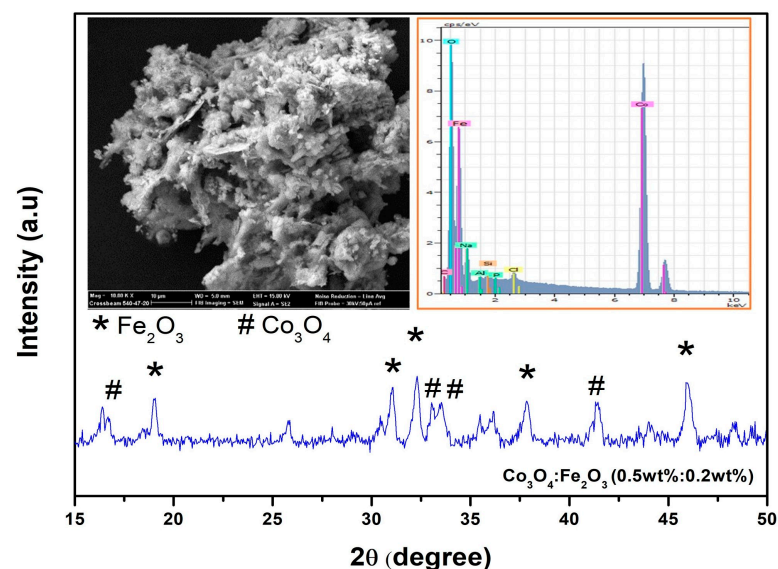
Figure 2. XRD pattern of prepared Co_3O_4:Fe_2O_3 (0.5 wt%:0.2 wt%) nanocomposite; insets show SEM and EDX of pure Co_3O_4 and Co_3O_4:Fe_2O_3 (0.5 wt%:0.4 wt%) nanocomposite.

XRD analysis showed the diffraction peaks of cubic Co_3O_4 and tetragonal Fe_2O_3, with space groups Fd3m and P, respectively, confirming that in the synthesized product cobalt oxide and iron oxide single-phase nanoparticles were present. SEM images showed that all the samples were composed of nanoparticles with an irregular shape. EDX spectra confirmed the presence of Co, Fe, and O in all the composite samples.

Additional characterization studies were also performed. First, BET surface area and porosity of the samples were evaluated by nitrogen adsorption and desorption isotherms at 77 K. A summary of the structural properties of the samples derived by N_2 adsorption-desorption isotherms, such as BET surface area, pore volume, and radius, are reported in Table 1. The data obtained provided evidence that the BET surface area was enhanced by increasing the amount of Fe_2O_3, reaching a maximum value for the nanocomposites with 0.2% of Fe_2O_3. It is noteworthy that the other structural parameters (i.e., pore volume

and pore radius) also changed with respect to the values associated with the pure oxides, reflecting the high interaction between them.

Table 1. Surface area, pore volume and pore radius for the pure Fe_2O_3, Co_3O_4 nanoparticles, and Fe_2O_3/Co_3O_4 nanocomposites.

| Samples	Surface Area m^2/g	Pore Volume cc/g	Pore Radius Å
Co_3O_4	59.63	0.141	17.165
X1: 0.1%	70.20	0.157	19.567
X2: 0.2%	91.66	0.186	16.529
X3: 0.3%	74.64	0.180	17.113
X4: 0.4%	73.85	0.128	16.493
X5: 0.5%	84.37	0.165	16.485
Fe_2O_3	53.90	0.102	17.304

ATR-FTIR spectra of pure Co_3O_4, Fe_2O_3, and Co_3O_4–Fe_2O_3 nanocomposites recorded in the wavenumber range from 500 to 4000 cm^{-1} are presented in Figure 3. The absorption peaks at 3485 cm^{-1}, 2929 cm^{-1}, and 2858 cm^{-1} were attributed to the –OH stretching, which agrees with the literature data [21–23]. The absorption peaks at 469 cm^{-1} and 654 cm^{-1} corresponding to the Fe-O stretch confirmed the successful synthesis of Co_3O_4–Fe_2O_3 nanocomposites, respectively.
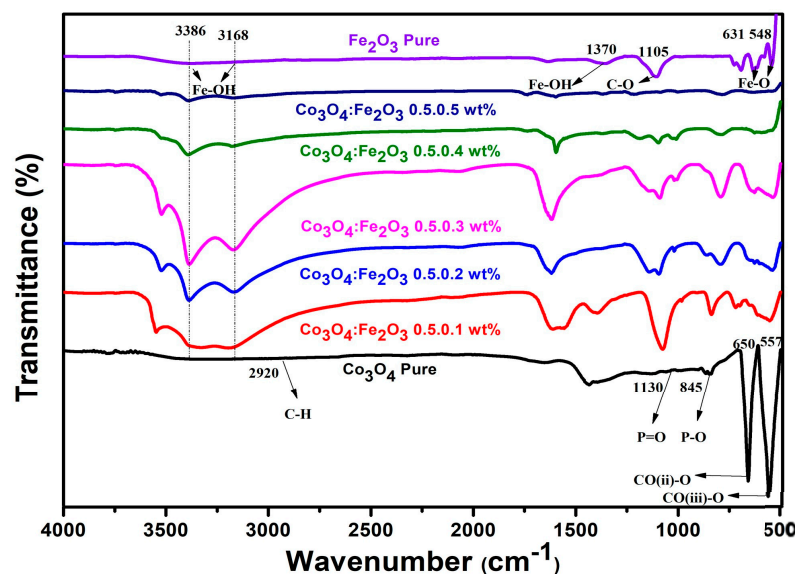
Figure 3. ATR-FTIR pattern of prepared Co_3O_4:Fe_2O_3 nanocomposites.

A Raman characterization (see Figure 4) was also performed. For the pure Fe_2O_3, four main Raman peaks were observed, in agreement with the other literature [24,25]. The Raman mode located at 218 cm^{-1} was identified for the A_{1g} mode while the vibrational Raman peaks related to E_g' modes were observed at 288 cm^{-1}, 401 cm^{-1} and 602 cm^{-1} [14,26]. According to Nagaraj et al., [25], E_g is due to the Fe–O stretching involving two iron and oxygen atoms. For pure Co_3O_4, we observed five major Raman modes. The three F_{2g} modes were located at 193 cm^{-1}, 516 cm^{-1}, and 613 cm^{-1} (F^2_{g1}, F^2_{g2}, F^2_{g3}, respectively) [24]. The peak at 474 cm^{-1} was assigned to the E_{2g} mode, while the one located at 682 cm^{-1} was assigned to A_{1g} [24,27,28]. Regarding the Co_3O_4:Fe_2O_3, by analogy with the work of Choya et al. [28], the influence of Fe_2O_3 in the Co_3O_4 lattice was analyzed based on the shift of the A_{1g} Raman mode observed at 682 cm^{-1} in the Co_3O_4 spectrum, which was considered as reference. According to this prior work, the redshift of the A_{1g} signal indicated spinel distortion [29]. In the composite samples, the full width at half maximum

(FWHM) of the A_{1g} Raman mode was also found to change in respect to pure Co_3O_4, i.e., it increased as the amount of Fe_2O_3 in the nanocomposite ratio grew (Figure 4b).
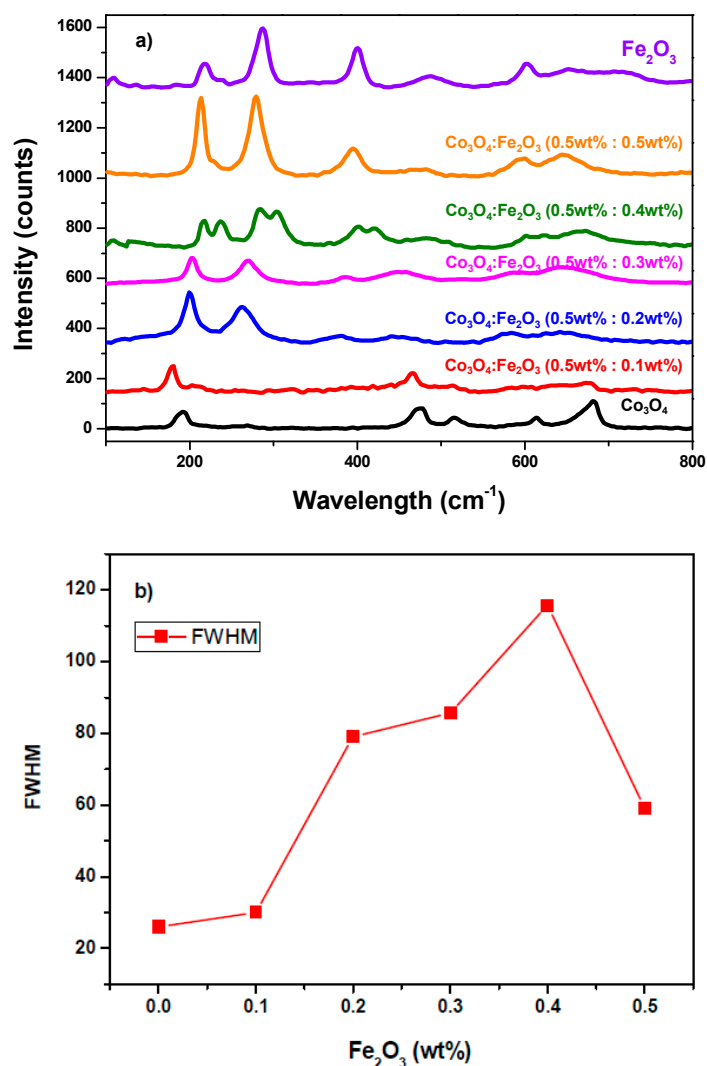
Figure 4. (**a**) Raman spectra of pure Fe_2O_3 (purple line), pure Co_3O_4 (black line), and Fe_2O_3:Co_3O_4 nanocomposites at different wt% ratio on SPCE using 16.6 mW power; (**b**) FWHM of A_{1g} Raman peak vs. the percentage of Fe in the nanocomposite.

The highest value of FWHM was obtained for Co_3O_4:Fe_2O_3 (0.5 wt%:0.4 wt%) which may have been due to a higher cobalt spinel distortion [29]. Moreover, a shift towards lower energies was observed for the F^2_{g2} and E_{2g} Raman modes while increasing the Fe_2O_3, which agreed with other works [24,27] and may be due to the effective interaction between the components of the Co_3O_4:Fe_2O_3 nanocomposite. Table 2 presents the vibrational Raman modes obtained in this work, compared with the literature, and their assignments.

Table 2. Raman vibrational modes.

Material	Raman Mode	Position	Ref
Fe_2O_3	A_{1g}	218 cm^{-1}	[24–26]
	$E_{g'}$	288 cm^{-1}, 401 cm^{-1} and 602 cm^{-1}	

Table 2. *Cont.*

Material	Raman Mode	Position	Ref
Co_3O_4	F^2_{g1}	193 cm^{-1}	[24]
	F^2_{g2}	516 cm^{-1}	
	F^2_{g3}	613 cm^{-1}	
	E_{2g}	474 cm^{-1}	[24,27,28]
	A_{1g}	682 cm^{-1}	
$Co_3O_4:Fe_2O_3$	A_{1g} F^2_{g2} $E_{g'}$	***	[24,27,29]

*** Raman peak positions when varying the ratio of $Co_3O_4:Fe_2O_3$. composites. A detailed explanation of their attribution is reported in the text.

3.2. Electrochemical Characterization of Modified SPCE

Cyclic voltametric (CV) and electrochemical impedance spectroscopy (EIS) tests were performed in 10 mM ferrocyanide solution ($K_3Fe(CN)_6$) for all modified electrodes. Figure 5a shows the Nyquist plot (i.e., plotting imaginary impedance ($-Z''$) versus real impedance (Z')) of the modified and unmodified electrodes in 10 mM ferrocyanide solution in PBS solution.

Using the fitting function by the Nova software, the equivalent circuit (Figure 5b) and the Randles parameters were determined and are reported in Table 3. Based on this EIS analysis, it is noteworthy that increasing the amount of Fe_2O_3 in the nanocomposite leads to a decrease in the circle radius, related to the charge transfer resistance R_{CT}, indicating the fast kinetic features of the composite-modified electrodes [30]. The conductivity feature is identified with the Randles parameter R_s. Modified electrodes display an increase in R_s value with respect to bare SPCEs, likely because of the greater distance of the solution from the electrode surface.
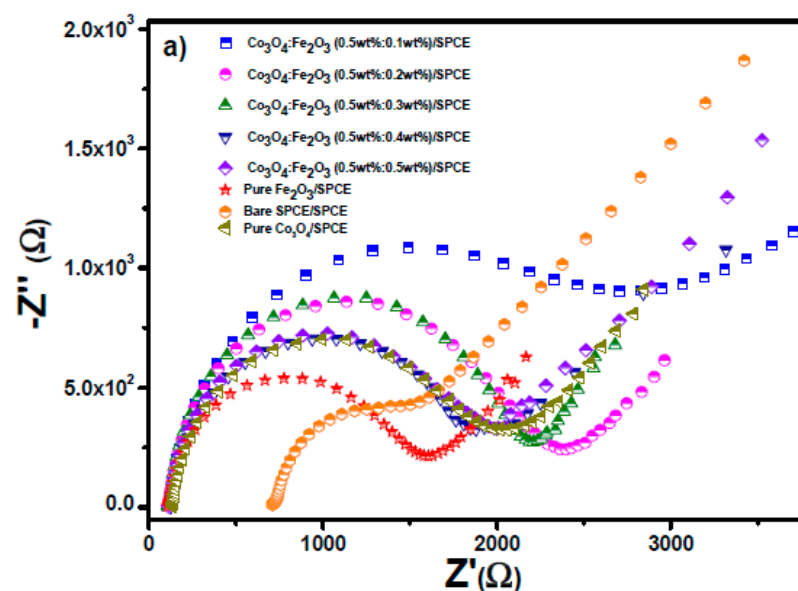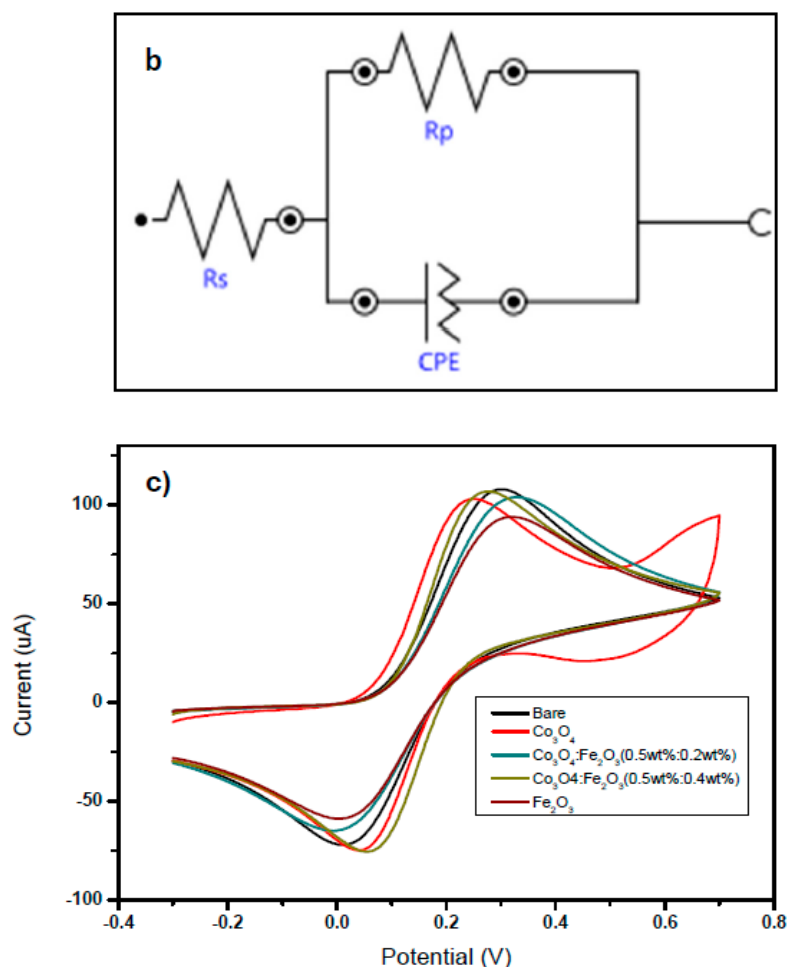

Figure 5. *Cont.*

Figure 5. (**a**) Nyquist plot of modified SPCE electrodes. (**b**) Equivalent circuit. (**c**) CV tests on the unmodified and modified electrodes carried out in 10 mM $[Fe(CN)_6]^{3-/4-}$ solution.

Table 3. Randles parameters of the modified electrodes.

Sensor	Randles Parameters	
	R_{CT} (Ω)	R_s (Ω)
Bare/SPCE	5022	46
Co_3O_4/SPCE	1923	109.4
Co_3O_4:Fe_2O_3 (0.5 wt%:0.1 wt%)/SPCE	2926	89.3
Co_3O_4:Fe_2O_3 (0.5 wt%:0.2 wt%)/SPCE	2080	111
Co_3O_4:Fe_2O_3 (0.5 wt%:0.3 wt%)/SPCE	2050	108.9
Co_3O_4:Fe_2O_3 (0.5 wt%:0.4 wt%)/SPCE	1801	115.3
Co_3O_4:Fe_2O_3 (0.5 wt%:0.5 wt%)/SPCE	1750	114.5
Fe_2O_3/SPCE	1423	103.9

Figure 5c reports the CV analysis carried out in 10 mM $[Fe(CN)_6]^{3-/4-}$ solution, in the −0.3–0.7 V potential range. It was noted that the addition of Fe_2O_3 improved the electrochemical characteristics (e.g., the oxidation/reduction peaks of $Fe(CN)_6]^{3-/4-}$ were narrower) of the bare SPCE and Co_3O_4–modified electrode.

Then, one more test was performed to select the best electrode for the detection of DA. First, we performed an optimization test to find the appropriate amount of the modifier to drop cast on the modified electrode (30, 50, 70 and 100 µL). The CV test was performed in a phosphate buffer solution (PBS, pH = 7.4, C = 0.01 M) containing 50 µM of DA. On all the modified SPCE electrodes, the anodic peak of DA was obtained at about 0.1 V. The highest oxidation peak current was obtained when modifying the working electrode with 50 µL.

When evaluating the response to 50 µM of dopamine, the best electrochemical performance was displayed by the $Co_3O_4:Fe_2O_3$(0.5 wt%:0.4 wt%) nanocomposite-based SPCE (see Figures 6 and S1).

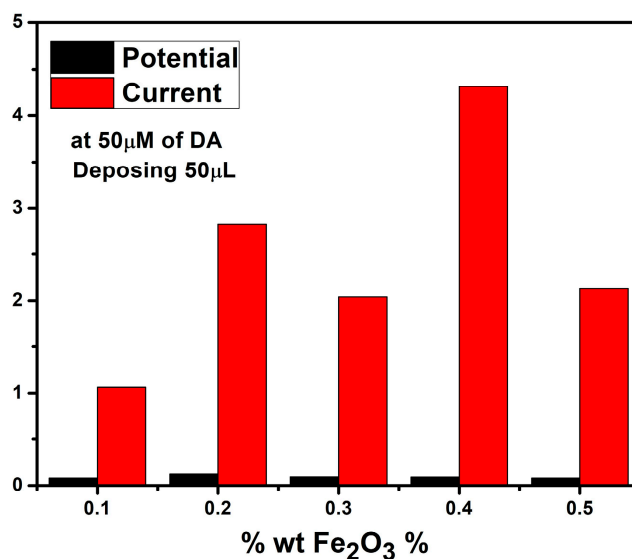**Figure 6.** Histogram of the response of the response to 50 µM of DA by the different Fe_2O_3 nanocomposites.

From these findings, the current decreased due to the variation in wt% of Fe_2O_3 from 0.1 to 0.3, and the potential increased due to the increase in the mass transport between the electrolyte and the electrode surface. Surprisingly, the current increased again to reach a higher value than that obtained with x = 0.1%, then decreased to a similar current value compared to Fe_2O_3 wt. 0.2%.

To discover if the electrochemical behavior of DA on $Co_3O_4:Fe_2O_3$ (0.5 wt%:0.4 wt%)/ SPCE is diffusion or adsorption controlled, the variation of scan rate versus anodic peak was plotted, see Figure 7a. Indeed, by increasing the scan rate from 0.02 to 0.4 V/s, a slight shift in the potential was noted, indicating that the mass transport had decreased. Figure 7b illustrates a linear variation of the scan rate root versus the anodic current with R^2 = 0.99 for both bare/SPCE and $Co_3O_4:Fe_2O_3$ (0.5 wt%:0.4 wt%)/SPCE. These findings show that the redox reaction was diffusion controlled for the prior electrode, see Figure 7b.
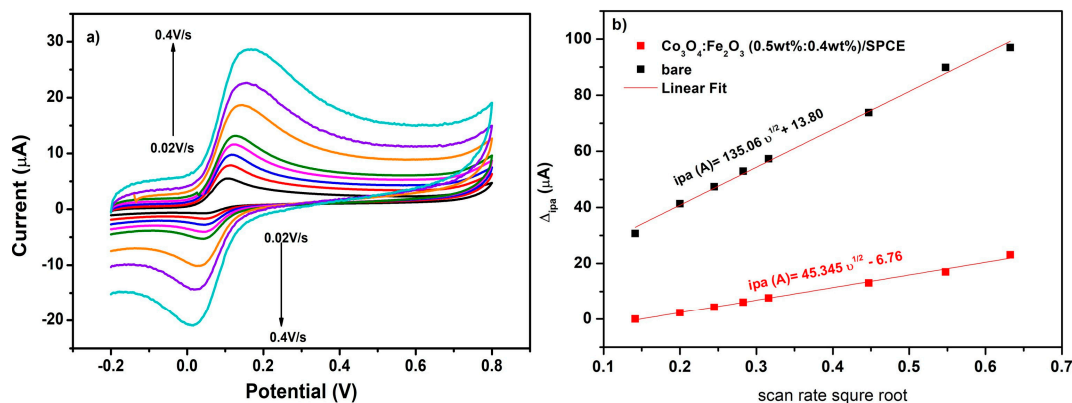

Figure 7. (**a**) Scan rate variation from 0.02 V/s to 0.4 V/s on $Co_3O_4:Fe_2O_3$ (0.5 wt%:0.4 wt%)/SPCE 100 µM of DA in 10 mM $Fe(CN)_6]^{3/4-}$; (**b**) current of anodic (black line) and cathodic (red line) peaks versus square root of scan rate.

According to previous work, we determined the active surface area (*A*) through the Randles-Sevcik equation [30]:

$$I_{pa} = 2.69 \times 10^5 A D^{1/2} n^{3/2} \nu^{1/2} C,$$

where *C* is the concentration in mol cm^{-3}, *n* is the number of electrons, ν is the scan rate, and *D* is the diffusion coefficient of the electrolyte [Fe(CN)$_6$]$^{3/4-}$ expressed in cm^2/s equal to 7.6×10^{-6} cm^2 s^{-1}. The anodic peak current (*I$_{pa}$*) is expressed in μA. From this equation, the active surface area of Co$_3$O$_4$:Fe$_2$O$_3$ was found to be 1.45×10^{-2} cm^{-2}, that is, almost 20 times greater compared to that of bare/SPCE.

3.3. Electroanalytical Dopamine Determination

Herein, we first tested the electroanalytical performance of two modified electrodes (Fe$_2$O$_3$/SPCE and Co$_3$O$_4$/SPCE) for the determination of DA compared with the bare SPCE electrode. The CV tests were performed in PBS solution containing different concentrations of DA ranging from 0 to 100 μM at [−0.2–0.8 V] potential range and 0.05 V/s scan rate. The results of this test are shown in the following Figure 8a–c. According to the results, the Co$_3$O$_4$/SPCE sensor displays the poorest electroanalytical behavior toward the redox reaction of dopamine while bare and Fe$_2$O$_3$/SPCE electrodes depict similar performance.

We also carried out a CV test under the same conditions on the Co$_3$O$_4$:Fe$_2$O$_3$ (0.5 wt%:0.4 wt%)/SPCE for the determination of DA at different concentrations, see Figure 8d. Compared to the bare and pure modified SPCE electrodes, Co$_3$O$_4$:Fe$_2$O$_3$ (0.5 wt%:0.4 wt%)/SPCE showed better electroanalytical performance where the DA Faradic current exhibited an increase of ~2-fold. Figure 8c presents the calibration curves of the modified and unmodified SPCEs electrodes where the peak current varied linearly with DA concentration. The regression equations of bare/SPCE, Fe$_2$O$_3$/SPCE, Co$_3$O$_4$/SPCE and Co$_3$O$_4$:Fe$_2$O$_3$ (0.5 wt%:0.4 wt%)/SPC are i$_{pa}$ (μA) = 0.047 + 0.103 C$_{DA}$ (μA), i$_{pa}$ (μA) = 0.048 + 0.099 C$_{DA}$ (μA), i$_{pa}$ (μA) = 0.016 + 0.119 C$_{DA}$ (μA), and i$_{pa}$ (μA) = 0.0736 + 0.1031 C$_{DA}$ (μA), respectively. The sensitivity (S) of this electrode was computed from the calibration curve, and the limit of detection (LOD) was determined by equation

$$\text{LOD} = 3.3 \, \text{SD}/\sigma,$$

where SD is the standard deviation and σ is the slope determined from the calibration curve, that were found to be 0.604 μA μM^{-1}cm^{-2} and 0.24 μM, respectively.

Based on the microstructural and electrochemical results obtained, we just report below a brief discussion of the electrochemical sensing mechanism of Co$_3$O$_4$–Fe$_2$O$_3$ heterojunctions. Figure 9 show the relationship between the FWHM value obtained by the above reported Raman measurements for the different Co$_3$O$_4$:Fe$_2$O$_3$ heterostructures and the response (defined by the current peak) to dopamine. This finding suggests that cobalt spinel distortion introduced by Fe$_2$O$_3$ is a key factor in enhancing the electrochemical characteristics for dopamine detection.

The distortion caused a change in the structural parameters of the composite heterostructures compared to the single metal oxides. Specifically, an increase in surface area was noted (see Table 1), leading to an enhancement in the number of more active sites. In any case, based on the other characterizations carried out, it cannot be excluded that other factors contributed to the enhanced response of the Co$_3$O$_4$:Fe$_2$O$_3$ heterostructures towards the target analyte. The superior sensing performances of the composites in comparison to the corresponding single phase metal oxides may indeed be due to the build-up of potential barriers at the p–n interface. The same finding was reported in other research. For example, because of the introduction of the p–n junction interface and the high catalytic activity of ZnO NPs, Liang and collaborators found that the sensitivity to DA was enhanced significantly [31]. Co$_3$O$_4$–Fe$_2$O$_3$ p–n heterojunctions have attracted much attention for improving gas-sensing performance [32,33] and for their excellent electrocatalytic activity for OER in alkaline solution [34], but no work has been reported about their use in electro-

chemical sensors. So, more detailed work is necessary to obtain the information that would be helpful in formulating a reliable hypothesis for the sensing mechanism. Nevertheless, considering the higher electron transfer or lower charge transfer resistance (see value of R_{CT} in Table 3) of the nanocomposite samples and, thus, the higher electrochemical activity, it can be assumed that p–n junctions play a decisive role in the sensing mechanism.
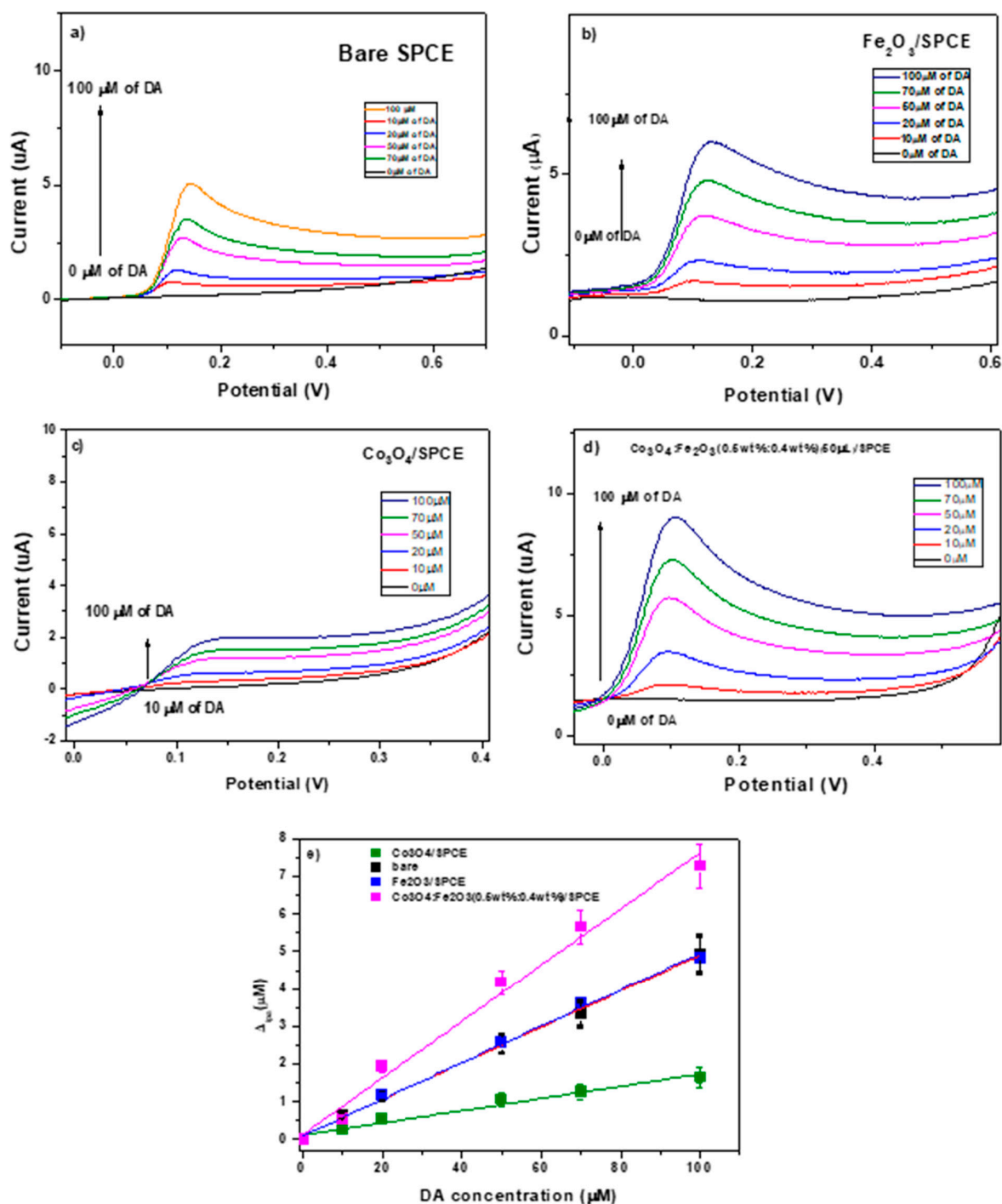
Figure 8. (**a**) CV test in the presence of DA on bare SPCE; (**b**) calibration curves vs. DA concentrations for SPCE, Fe_2O_3/SPCE, and Co_3O_4/SPCE; (**c**) CV test in the presence of DA on Co_3O_4:Fe_2O_3 (0.5 wt%:0.4 wt%)/SPCE, and (**d**) comparison of calibration curves of modified and unmodified electrodes. (**e**) calibration curve.
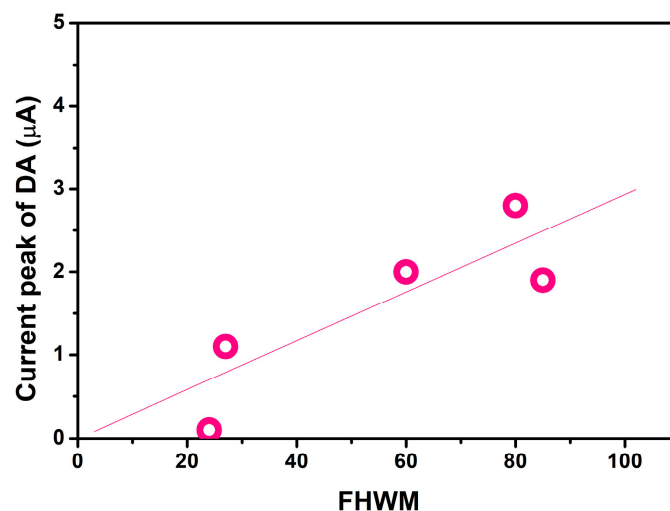
Figure 9. Relationship between the FWHM value obtained for the various Co_3O_4:Fe_2O_3 heterostructures and the response to dopamine.

Summarizing, the results obtained may be due to all these factors: (i) the increase in surface area which also improves the DA approach to the electrode surface; (ii) the formation of numerous and more active sites at the Co_3O_4:Fe_2O_3 interface; (iii) the improved electrical properties due to p–n junctions. Hence, a plausible sensing mechanism for dopamine detection implies that the target analyte adsorbs easily and in higher quantity on the Co_3O_4:Fe_2O_3 heterostructure hybrid nanoparticles. Better interaction between the heterostructured electrocatalyst and DA leads to better oxidation and sensitive detection. This step also helps to activate the hydroxyl group of DA towards electro-oxidation, thus, resulting in an improved electron transfer with the electrode. Overall, the formation of the Co_3O_4:Fe_2O_3 heterostructure reduces the impedance and increases the availability of electrons which is the crucial step for electrochemical sensing.

A comparison of the analytical parameters for the detection of DA on our modified electrode with previous sensors reported in the literature is presented in Table 4, below. Based on these reference papers, the performances of the proposed modified electrode are good, also considering the simple materials used and its easy and cost-effective preparation.

Table 4. Comparison of the analytical parameters of our modified electrode and previous sensors reported in the literature for the detection of DA.

Sensor	Analyte	LOD (µM)	Sensitivity	Analytical Technique	Ref.
WS_2 NSs-CNFs	DA	0.01	5.36 $\mu M^{-1} cm^{-2}$	DPV	[35]
α-Fe_2O_3 NPs/CC	DA	0.074–113	0.020 $\mu M^{-1} cm^{-2}$	CV	[36]
Fe_3O_4/GO/PG	DA	0.01	5.96 $\mu M^{-1} cm^{-2}$	DPV	[37]
Urchin-WO_3/SPCE	DA	0.25	55.9 $\mu A/\mu M^{-1} cm^{-2}$	DPV	[38]
Fe_3O_4/rGO/GCE	DA	0.12	2.733 $\mu A/\mu M^{-1}$	DPV	[39]
SPCE$-Fe_3O_4$/SPEEK	DA	7.1	0.005 $\mu A/\mu M$	SWV/CV	[40]
Co_3O_4/$NiCo_2O_4$	DA	0.24	–	CV	[41]
RS AuNPs/SPCE	DA	0.2	550.4 $\mu A/\mu M^{-1} cm^{-2}$	LSV	[42]
Co_3O_4:Fe_2O_3/SPCE	DA	0.241	0.604 $\mu A/\mu M^{-1} cm^{-2}$	CV	This work

3.4. Interference Tests

In addition to the good electrochemical response toward DA determination observed with Co_3O_4:Fe_2O_3 (0.5 wt%:0.4 wt%)/SPCE, we checked the response to analytes other than DA in 0.01 M PBS solution and at a scan rate of 0.05 V/s. The chosen analytes were uric acid (UA), folic acid (FA), and L-tyrosine. As depicted in Figure 10a, the tyrosine (Tyr) oxidation peak can be clearly observed on the modified electrode at ~0.6 V. The DA faradic current

remained constant when increasing L-Tyr concentration from 20 to 200 μM. In Figure 10b, after widening the potential applied up to 1.1 V, we also observed the oxidation peak at ~0.8 V, due to the redox Fe^{2+}/Fe^{3+} process [43] and FA (~1.0 V) added as another analyte. As shown, also after the addition of all these analytes, the peak current related to dopamine remained well stable.
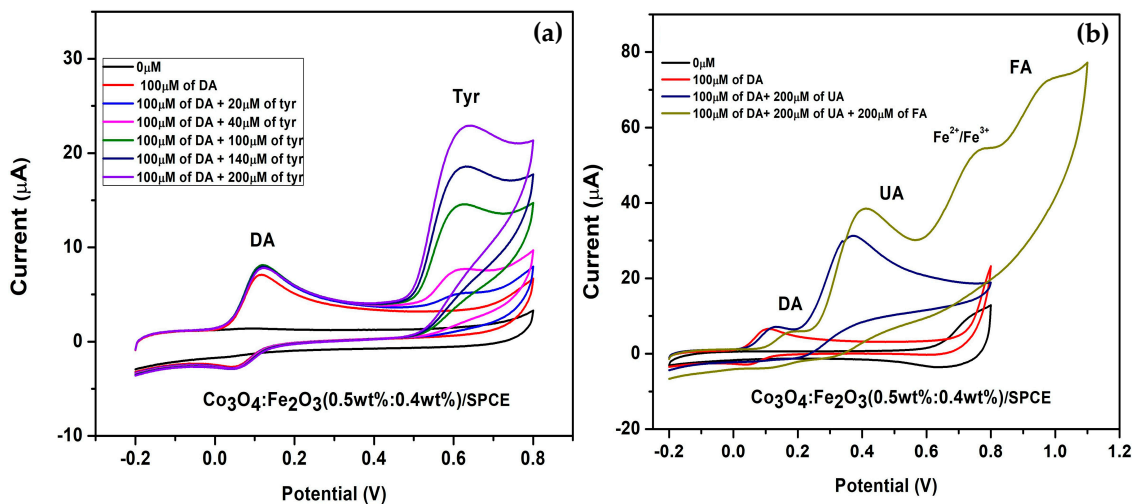
Figure 10. Selectivity test of $Co_3O_4:Fe_2O_3$ (0.5 wt%:0.4 wt%)/SPCE in PBS containing 100 μM of DA and (**a**) L-Tyrosine at different concentrations ranging from 0 to 100 μM, (**b**) 200 μM of UA and 200 μM of FA.

The above tests are helpful, anyway, when trying to develop a practical sensor for dopamine detection. These future studies are planned with the primary objective of optimizing the performance for dopamine detection in order to develop a practical sensor.

4. Conclusions

In this paper, we modified SPCEs using different $Co_3O_4:Fe_2O_3$ heterojunctions and tested them toward the determination of DA. Through this study, the formation of $Co_3O_4:Fe_2O_3$ (0.5 wt%:0.4 wt%) resulted in a nanocomposite with the best performance in the determination of DA. Using this modified SPCE, an increment in the faradic current towards DA was observed when compared to unmodified and other modified $Co_3O_4:Fe_2O_3$/SPCEs with a sensitivity and limit of detection (LOD) equal to 0.604 μA μM^{-1}cm^{-2} and 0.24 μM, respectively. This modified electrode showed further good selectivity toward L-Tyr, UA, and riboflavin. These results were attributed to the formation of $Co_3O_4:Fe_2O_3$ heterostructures, as confirmed by XRD, Raman, and FTIR characterization analysis. The enhanced-sensing mechanism was also discussed, which could be explained by the synergistic effects induced by the larger specific surface area and consequently an enhanced adsorption of DA compared to the single metal oxides. The p–n junction formed also played a key role in enhancing the electrochemical response to DA. Due to the above-reported promising results, we plan future studies with the objective of optimizing the performance of dopamine detection and try to develop a sensor for practical application in clinical medicine.

References

1. Moujalled, D.; Strasser, A.; Liddell, J.R. Molecular Mechanisms of Cell Death in Neurological Diseases. *Cell Death Differ.* **2021**, *28*, 2029–2044. [CrossRef] [PubMed]
2. Pan, X.; Kaminga, A.C.; Wen, S.W.; Wu, X.; Acheampong, K.; Liu, A. Dopamine and Dopamine Receptors in Alzheimer's Disease: A Systematic Review and Network Meta-Analysis. *Front. Aging Neurosci.* **2019**, *11*, 175. [CrossRef] [PubMed]
3. Grant, C.E.; Flis, A.L.; Ryan, B.M. Understanding the Role of Dopamine in Cancer: Past, Present and Future. *Carcinogenesis* **2022**, *43*, 517–527. [CrossRef] [PubMed]
4. Lakard, S.; Pavel, I.-A.; Lakard, B. Electrochemical Biosensing of Dopamine Neurotransmitter: A Review. *Biosensors* **2021**, *11*, 179. [CrossRef]
5. Grieshaber, D.; MacKenzie, R.; Vörös, J.; Reimhult, E. Electrochemical Biosensors—Sensor Principles and Architectures. *Sensors* **2008**, *8*, 1400–1458. [CrossRef]
6. Sargazi, S.; Fatima, I.; Hassan Kiani, M.; Mohammadzadeh, V.; Arshad, R.; Bilal, M.; Rahdar, A.; Díez-Pascual, A.M.; Behzadmehr, R. Fluorescent-Based Nanosensors for Selective Detection of a Wide Range of Biological Macromolecules: A Comprehensive Review. *Int. J. Biol. Macromol.* **2022**, *206*, 115–147. [CrossRef]
7. Taheri, R.A.; Eskandari, K.; Negahdary, M. An Electrochemical Dopamine Aptasensor Using the Modified Au Electrode with Spindle-Shaped Gold Nanostructure. *Microchem. J.* **2018**, *143*, 243–251. [CrossRef]
8. Varmira, K.; Mohammadi, G.; Mahmoudi, M.; Khodarahmi, R.; Rashidi, K.; Hedayati, M.; Goicoechea, H.C.; Jalalvand, A.R. Fabrication of a Novel Enzymatic Electrochemical Biosensor for Determination of Tyrosine in Some Food Samples. *Talanta* **2018**, *183*, 1–10. [CrossRef]
9. Ferlazzo, A.; Espro, C.; Iannazzo, D.; Neri, G. Determination of Phenylalanine by a Novel Enzymatic PHD/SPE Biosensor. *IEEE Trans. Instrum. Meas.* **2023**, *72*, 9508308. [CrossRef]
10. Abid, K.; Zribi, R.; Maalej, R.; Foti, A.; Khaskhoussi, A.; Gucciardi, P.G.; Neri, G. Electrochemical and Sensing Properties of AuNps-2D-MoS2/SPCE for Folic Acid Determination. *FlatChem* **2022**, *36*, 100433. [CrossRef]
11. Okpara, E.C.; Nde, S.C.; Fayemi, O.E.; Ebenso, E.E. Electrochemical Characterization and Detection of Lead in Water Using SPCE Modified with BiONPs/PANI. *Nanomaterials* **2021**, *11*, 1294. [CrossRef]
12. Neri, G. First Fifty Years of Chemoresistive Gas Sensors. *Chemosensors* **2015**, *3*, 1. [CrossRef]
13. Fazio, E.; Spadaro, S.; Corsaro, C.; Neri, G.; Leonardi, S.G.; Neri, F.; Lavanya, N.; Sekar, C.; Donato, N.; Neri, G. Metal-Oxide Based Nanomaterials: Synthesis, Characterization and Their Applications in Electrical and Electrochemical Sensors. *Sensors* **2021**, *21*, 2494. [CrossRef] [PubMed]
14. Liu, L.; Wang, Y.; Liu, Y.; Wang, S.; Li, T.; Feng, S.; Qin, S.; Zhang, T. Heteronanostructural Metal Oxide-Based Gas Microsensors. *Microsyst. Nanoeng.* **2022**, *8*, 85. [CrossRef] [PubMed]
15. Kumarage, G.W.C.; Comini, E. Low-Dimensional Nanostructures Based on Cobalt Oxide (Co$_3$O$_4$) in Chemical-Gas Sensing. *Chemosensors* **2021**, *9*, 197. [CrossRef]
16. Sun, C.; Huang, H.; Wang, J.; Liu, W.; Yang, Z.; Yu, X.-F. Applications of Electrochemical Biosensors Based on 2D Materials and Their Hybrid Composites in Hematological Malignancies Diagnosis. *Technol. Cancer Res. Treat.* **2022**, *21*, 15330338221142996. [CrossRef]
17. Agnihotri, A.S.; Varghese, A.; Nidhin, M. Transition Metal Oxides in Electrochemical and Bio Sensing: A State-of-Art Review. *Appl. Surf. Sci. Adv.* **2021**, *4*, 100072. [CrossRef]
18. Zhou, Z.; Liu, X.; Chan, H. Synthesis of Fe$_3$O$_4$ Nanoparticles from Emulsions. *J. Mater. Chem.* **2001**, *11*, 1704–1709. [CrossRef]
19. Wu, W.; Wu, Z.; Yu, T.; Jiang, C.; Kim, W.-S. Recent Progress on Magnetic Iron Oxide Nanoparticles: Synthesis, Surface Functional Strategies and Biomedical Applications. *Sci. Technol. Adv. Mater.* **2015**, *16*, 023501. [CrossRef]
20. Choi, H.K.; Lee, M.-J.; Lee, S.N.; Kim, T.-H.; Oh, B.-K. Noble Metal Nanomaterial-Based Biosensors for Electrochemical and Optical Detection of Viruses Causing Respiratory Illnesses. *Front. Chem.* **2021**, *9*, 672739. [CrossRef]

21. Chen, W.; Yi, P.; Zhang, Y.; Zhang, L.; Deng, Z.; Zhang, Z. Composites of Aminodextran-Coated Fe$_3$O$_4$ Nanoparticles and Graphene Oxide for Cellular Magnetic Resonance Imaging. *ACS Appl. Mater. Interfaces* **2011**, *3*, 4085–4091. [CrossRef]

22. Izadiyan, Z.; Shameli, K.; Miyake, M.; Hara, H.; Mohamad, S.E.B.; Kalantari, K.; Taib, S.H.M.; Rasouli, E. Cytotoxicity Assay of Plant-Mediated Synthesized Iron Oxide Nanoparticles Using Juglans Regia Green Husk Extract. *Arab. J. Chem.* **2020**, *13*, 2011–2023. [CrossRef]

23. Qin, H.; Wang, C.M.; Dong, Q.Q.; Zhang, L.; Zhang, X.; Ma, Z.Y.; Han, Q.R. Preparation and Characterization of Magnetic Fe$_3$O$_4$–Chitosan Nanoparticles Loaded with Isoniazid. *J. Magn. Magn. Mater.* **2015**, *381*, 120–126. [CrossRef]

24. Bhushan, M.; Kumar, Y.; Periyasamy, L.; Viswanath, A.K. Antibacterial Applications of α-Fe$_2$O$_3$/Co$_3$O$_4$ Nanocomposites and Study of Their Structural, Optical, Magnetic and Cytotoxic Characteristics. *Appl. Nanosci.* **2018**, *8*, 137–153. [CrossRef]

25. Basavegowda, N.; Mishra, K.; Rok Lee, Y. Synthesis, Characterization, and Catalytic Applications of Hematite (α-Fe$_2$O$_3$) Nanoparticles as Reusable Nanocatalyst. *Adv. Nat. Sci. Nanosci. Nanotechnol.* **2017**, *8*, 025017. Available online: https://iopscience.iop.org/article/10.1088/2043-6254/aa6885 (accessed on 29 June 2023). [CrossRef]

26. Lu, J.-F.; Tsai, C.-J. Hydrothermal Phase Transformation of Hematite to Magnetite. *Nanoscale Res. Lett.* **2014**, *9*, 230. [CrossRef]

27. Li, J.; Lu, G.; Wu, G.; Mao, D.; Guo, Y.; Wang, Y.; Guo, Y. The Role of Iron Oxide in the Highly Effective Fe-Modified Co$_3$O$_4$ Catalyst for Low-Temperature CO Oxidation. *RSC Adv.* **2013**, *3*, 12409–12416. [CrossRef]

28. Farhadi, S.; Javanmard, M.; Nadri, G. Characterization of Cobalt Oxide Nanoparticles Prepared by the Thermal Decomposition. *Acta Chim. Slov.* **2016**, *63*, 335–343. [CrossRef]

29. Choya, A.; de Rivas, B.; Gutiérrez-Ortiz, J.I.; González-Velasco, J.R.; López-Fonseca, R. Synthesis, Characterization and Kinetic Behavior of Supported Cobalt Catalysts for Oxidative after-Treatment of Methane Lean Mixtures. *Materials* **2019**, *12*, 3174. [CrossRef]

30. Laschuk, N.; Easton, E.; Zenkina, O. Reducing the Resistance for the Use of Electrochemical Impedance Spectroscopy Analysis in Materials Chemistry. *RSC Adv.* **2021**, *11*, 27925–27936. [CrossRef]

31. Liang, J.-J.; Zhao, M.-G.; Ding, L.-J.; Fan, S.-S.; Chen, S.-G. Fabrication of the ZnO/NiO p–n Junction Foam for the Enhanced Sensing Performance. *Chin. Chem. Lett.* **2017**, *28*, 670–674. [CrossRef]

32. Xu, K.; Gao, J.; Chen, P.; Zhan, C.; Yang, Y.; Wang, Z.; Yang, Y.; Yang, L.; Yuan, C. Interface Engineering of Fe$_2$O$_3$@Co$_3$O$_4$ Nanocubes for Enhanced Triethylamine Sensing Performance. *Ind. Eng. Chem. Res.* **2022**, *61*, 8057–8068. [CrossRef]

33. Xu, K.; Zhao, W.; Yu, X.; Duan, S.; Zeng, W. MOF-derived Co$_3$O$_4$/Fe$_2$O$_3$ p-n hollow cubes for improved acetone sensing characteristics. *Phys. E Low Dimens. Syst. Nanostruct.* **2020**, *118*, 113869. [CrossRef]

34. Yue, H.Y.; Wu, P.F.; Huang, S.; Gao, X.; Song, S.S.; Wang, W.Q.; Zhang, H.J.; Guo, X.R. Electrochemical Determination of Dopamine in the Presence of Uric Acid Using WS2 Nanospheres-Carbon Nanofibers. *J. Electroanal. Chem.* **2019**, *833*, 427–432. [CrossRef]

35. Mahesh, K.P.O.; Shown, I.; Chen, L.-C.; Chen, K.-H.; Tai, Y. Flexible Sensor for Dopamine Detection Fabricated by the Direct Growth of α-Fe$_2$O$_3$ Nanoparticles on Carbon Cloth. *Appl. Surf. Sci.* **2018**, *427*, 387–395. [CrossRef]

36. Yang, Y.; Zhu, C.; Zhang, Y.; Xie, Y.; Lv, L.; Chen, W.; He, Y.; Hu, Z. Construction of Co$_3$O$_4$/Fe$_2$O$_3$ nanosheets on nickel foam as efficient electrocatalyst for the oxygen evolution reaction. *J. Phys. Chem. Solids* **2021**, *148*, 109680. [CrossRef]

37. Cai, L.; Hou, B.; Shang, Y.; Xu, L.; Zhou, B.; Jiang, X.; Jiang, X. Synthesis of Fe$_3$O$_4$/Graphene Oxide/Pristine Graphene Ternary Composite and Fabrication Electrochemical Sensor to Detect Dopamine and Hydrogen Peroxide. *Chem. Phys. Lett.* **2019**, *736*, 136797. [CrossRef]

38. Oğuz, M.; Aykaç, A.; Sen, M. Highly Sensitive and Selective Electrochemical Detection of Dopamine and Uric Acid Using Sea Urchin-like Tungsten Oxide Nanostructure Modified SPCE. *ChemRxiv* **2020**, *3*, 2011–2023. [CrossRef]

39. Peik-See, T.; Pandikumar, A.; Nay-Ming, H.; Hong-Ngee, L.; Sulaiman, Y. Simultaneous Electrochemical Detection of Dopamine and Ascorbic Acid Using an Iron Oxide/Reduced Graphene Oxide Modified Glassy Carbon Electrode. *Sensors* **2014**, *14*, 15227–15243. [CrossRef]

40. Ranku, M.N.; Uwaya, G.E.; Fayemi, O.E. Electrochemical Detection of Dopamine at Fe$_3$O$_4$/SPEEK Modified Electrode. *Molecules* **2021**, *26*, 5357. [CrossRef]

41. Liu, T.; Zhang, X.; Fu, K.; Zhou, N.; Xiong, J.; Su, Z. Fabrication of Co$_3$O$_4$/NiCo$_2$O$_4$ Nanocomposite for Detection of H$_2$O$_2$ and Dopamine. *Biosensors* **2021**, *11*, 452. [CrossRef]

42. Chelly, S.; Chelly, M.; Zribi, R.; Gdoura, R.; Bouaziz-Ketata, H.; Neri, G. Electrochemical Detection of Dopamine and Riboflavine on a Screen-Printed Carbon Electrode Modified by AuNPs Derived from Rhanterium Suaveolens Plant Extract. *ACS Omega* **2021**, *6*, 23666–23675. [CrossRef]

43. Kabtamu, D.M.; Lin, G.-Y.; Chang, Y.-C.; Chen, H.-Y.; Huang, H.-C.; Hsu, N.-Y.; Chou, Y.-S.; Wei, H.-J.; Wang, C.-H. The Effect of Adding Bi^{3+} on the Performance of a Newly Developed Iron–Copper Redox Flow Battery. *RSC Adv.* **2018**, *8*, 8537–8543. [CrossRef]